Chemical Engineering Journal 512 (2025) 162204

Contents lists available at ScienceDirect

Chemical Engineering Journal

journal homepage: www.elsevier.com/locate/cej

Unravelling degradation mechanisms of anion exchange membrane direct ammonia fuel cells via distribution of relaxation times

Wenzhi Li [a], Qing Wang [a], Yun Liu [a], Lizhen Wu [a], Zhefei Pan [b,c,*], Rong Chen [b,c,**], Liang An [a,d,***]

[a] Department of Mechanical Engineering, The Hong Kong Polytechnic University, Hung Hom, Kowloon, Hong Kong Special Administrative Region
[b] Key Laboratory of Low-grade Energy Utilization Technologies and Systems (Chongqing University), Ministry of Education of China, Chongqing University, Chongqing 400044, China
[c] Institute of Engineering Thermophysics, School of Energy and Power Engineering, Chongqing University, Chongqing 400044, China
[d] Research Institute for Smart Energy, The Hong Kong Polytechnic University, Hung Hom, Kowloon, Hong Kong Special Administrative Region

ARTICLE INFO

Keywords:
Direct ammonia fuel cells
Degradation mechanisms
Distribution of relaxation times
Ammonia oxidation
Ammonia crossover

ABSTRACT

Anion-exchange membrane direct ammonia fuel cells (AEM-DAFCs) have garnered increasing attention due to their carbon-free properties. However, they are not yet ready for widespread application because of their poor stability (< 80 h) and low power density (< 420 mW cm^{-2}). Additionally, the mechanisms behind cell performance degradation remain unclear. This study is the first to utilize electrochemical impedance spectroscopy (EIS) combined with distribution of relaxation times (DRT) analysis to thoroughly investigate the degradation mechanisms of AEM-DAFCs. DRT is a non-parametric model that effectively interprets EIS spectra by translating them from the frequency domain to the time domain, allowing for the distinction of overlapping polarization processes. Operating conditions assist in identifying the characteristic peaks obtained by DRT, which correspond to the kinetics of the ammonia oxidation reaction (AOR), the kinetics of the oxygen reduction reaction (ORR), and ionic transport. During a 50-hour stability test, in addition to interpreting EIS spectra with DRT, a reference electrode is used to separate the overpotential losses of the anode and cathode. Post-characterization tests are also conducted to examine changes in the electrode microstructure and composition before and after the stability test. The results indicate that cell performance decay primarily stems from the deterioration of AOR kinetics, specifically due to the dissolution (particularly of iridium), migration, and agglomeration of the PtIr/C catalyst, as well as poisoning by adsorbed species such as *N and *NO_x. These findings elucidate the mechanisms of cell performance degradation and provide guidance for the development of highly stable AEM-DAFCs.

1. Introduction

Anion-exchange membrane direct ammonia fuel cells (AEM-DAFCs) have emerged as a promising zero-carbon power generation technology, combining advantages such as low-temperature operation (<120 °C), rapid start-up capability, and compact zero-gap configuration [1,2]. Compared to hydrogen, ammonia can be liquefied under moderate conditions (only 10 bar at ambient temperature) and it also benefits from an established storage and transportation infrastructure, substantially reducing fuel handling cost [3,4]. Economically, ammonia is 31 % cheaper than hydrogen, with source-to-tank costs of \$4.5 GGE^{-1} compared to \$6.55 GGE^{-1} [5]. The integration of technical feasibility and economic competitiveness establishes ammonia as a promising alternative to hydrogen for fuel cell applications.

In 2010, Professor Tao's research group at the University of Warwick first incorporated an anion exchange membrane (AEM) into direct ammonia fuel cells (DAFCs), achieving a peak power density of 16 mW cm^{-2} [6]. This milestone confirmed the feasibility of AEM-DAFCs and

* Corresponding author at: Key Laboratory of Low-grade Energy Utilization Technologies and Systems (Chongqing University), Ministry of Education of China, Chongqing University, Chongqing 400044, China.
** Corresponding author at: Key Laboratory of Low-grade Energy Utilization Technologies and Systems (Chongqing University), Ministry of Education of China, Chongqing University, Chongqing 400044, China.
*** Corresponding author at: Department of Mechanical Engineering, The Hong Kong Polytechnic University, Hung Hom, Kowloon, Hong Kong Special Administrative Region.
E-mail addresses: zhefei.pan@cqu.edu.cn (Z. Pan), rchen@cqu.edu.cn (R. Chen), liang.an@polyu.edu.hk (L. An).

https://doi.org/10.1016/j.cej.2025.162204
Received 5 January 2025; Received in revised form 28 March 2025; Accepted 31 March 2025
Available online 4 April 2025

advanced their development. However, the progress in AEM-DAFCs was still hindered by poor conductivity and durability of AEMs, leading to high ohmic loss and limited stability [7]. A breakthrough came in 2019 when Professor Yan's research group at the University of Delaware developed a poly(aryl piperidinium) AEM with an ionic conductivity of 193 mS cm^{-1} at 95 °C, together with robust mechanical properties and enhanced chemical stability [8]. By incorporating this advanced AEM into DAFCs, they achieved a remarkable peak power density of 135 mW cm^{-2} [5]. Further optimization of operating conditions and the use of an ammonia-tolerant $MnCo_2O_4$ cathode catalyst boosted the power density to reach 410 mW cm^{-2} [9]. Despite these advancements, the practical application of this technology in portable devices remains challenging due to their limited operation stability. To date, the longest operation of AEM-DAFCs is only 80 h, which falls short of the requirements for practical applications [9]. Liu et al. [10] demonstrated the feasibility of AEM-DAFCs by achieving stable operation for over 25 h, but with a voltage decay exceeding 200 mV. Wang et al. [11] improved the durability of DAFCs by developing a cell with a Pd/C cathode, enabling continuous operation for up to 36 h at a current density of 300 mA cm^{-2}, with a decay rate of approximately 1 mV h^{-1}. Also, they confirmed via XPS analysis that Pd dissolution contributed to this performance loss. Based on this work, Wang et al. [9] further enhanced durability by incorporating a PTFE-containing cathode, achieving an 80-hour continuous operation at 300 mA cm^{-2} with an average voltage decay rate of 1.6 mV h^{-1}. The decrease in cell voltage and the increase in ohmic resistance are primarily attributed to the chemical degradation of the membrane under harsh operation conditions (3.0 M KOH and 100 °C). Additionally, the deactivation of ammonia oxidation reaction (AOR) catalysts, caused by the formation of strongly adsorbed intermediates during ammonia oxidation [12,13]. However, current research on the stability of AEM-DAFCs remains severely inadequate, and there is a lack of systematic understanding of the mechanisms behind performance degradation. Specifically, there is a lack of quantitative assessment of key factors contributing to performance decay, such as anode catalyst poisoning [14,15] (leading to increased activation overpotential for the AOR), chemical decomposition of AEMs [9,16] (leading to higher ohmic resistance), and ammonia crossover [17–19] (restricting kinetics of oxygen reduction). Therefore, it is crucial to utilize advanced diagnostic techniques to systematically analyze AEM-DAFCs, identify the root causes of performance degradation, and develop targeted strategies to enhance their stability.

To address these challenges, advanced diagnostic tools are needed to decouple the complicated degradation mechanisms. Electrochemical impedance spectroscopy (EIS) is a non-destructive and in-situ diagnostic tool, which has been widely used to separate different polarization processes in electrochemical systems [20,21]. Interpreting EIS data often requires fitting it to suitable equivalent circuit models, which demands prior knowledge and introduces complexity and uncertainty into the analysis [22,23]. Identifying specific characteristics within the EIS spectra can also be challenging, especially when multiple processes overlap in the frequency domain [24]. To overcome these challenges, the distribution of relaxation times (DRT) method can be employed. By converting EIS data from the frequency domain to the time domain, DRT effectively separates processes with similar time constants, simplifying the interpretation of EIS results [25,26]. The DRT approach has been successfully applied to diagnose and evaluate various electrochemical systems, including fuel cells [27,28], lithium-ion batteries [29,30] and water electrolyzers [31,32]. Moreover, this method holds promise for providing deeper insights into the degradation mechanisms of AEM-DAFCs, thereby enhancing their stability and performance.

In this study, we conduct a comprehensive investigation into the factors affecting the stability of AEM-DAFCs. Our approach combines electrochemical measurements with electrode characterizations to elucidate the underlying degradation mechanisms. Specifically, we employ EIS with DRT analysis to effectively separate and identify the losses occurring during stability tests. This method allows us to categorize losses into AOR kinetic losses, ORR kinetic losses, and ionic transport losses, beyond merely assessing ohmic losses. By monitoring the evolution of these characteristic peaks, we highlight the primary factors contributing to cell degradation. Furthermore, we utilize reference electrodes to measure variations in anode overpotential, enabling us to discern the contributions of both anode and cathode overpotentials to the overall cell voltage decay. To further support our findings, we employ scanning electron microscopy (SEM) and energy dispersive spectrometry (EDS) to analyze microstructural changes in the aged cell, providing additional evidence to explain the degradation process. In summary, this work offers a detailed analysis of the mechanisms causing cell voltage degradation during stability tests, providing valuable insights for enhancing the operation stability of AEM-DAFCs.

2. Experimental

2.1. Fuel cell fabrication

The membrane electrode assembly (MEA) used in this study consists of an anode, a cathode, and an anion exchange membrane separating the two electrodes, with an active area of 2.0 × 2.0 cm^2. The anode electrode is composed of a diffusion layer and a catalyst layer. The diffusion layer is a carbon cloth (HCP330N, Shanghai Hesen Co., China). The catalyst layer was formed by spraying a well-dispersed catalyst ink onto the carbon cloth at 80 °C. The ink was made by mixing the PtIr/C catalyst (40 % PtIr on Vulcan XC-72R, Pt/Ir = 1:1, Premetek Co., USA) and Nafion ionomer (5 wt%, D520, DuPont Co., USA) in a 4:1 mass ratio, using ethanol as the solvent. This mixture was ultrasonicated for 30 min in an ice-water bath. The catalyst loading on the anode electrode is 2.0 mg cm^{-2}, providing sufficient active sites for the ammonia oxidation reaction. The cathode electrode also consists of a diffusion layer and a catalyst layer. The diffusion layer is a carbon paper (TGP-H-090, Toray Co., Japan). The catalyst layer was applied by spraying a well-dispersed ink onto the carbon paper at 80 °C. The ink was prepared by combining a Pt/C catalyst (60 %, Premetek Co., USA) and Nafion ionomer (5 wt%, D520, DuPont Co., USA) in a 4:1 mass ratio, with ethanol as the solvent. This mixture was ultrasonicated for 30 min in an ice-water bath. The catalyst loading on the cathode electrode is 1.0 mg cm^{-2}, providing ample active sites for the oxygen reduction reaction. The commercial PiperION^{TM} membrane (Versogen Co., USA) was used to facilitate OH^- conduction. Prior to cell assembly, the membrane was pre-treated in 1.0 M KOH at room temperature for 24 h.

2.2. Electrochemical measurements

For electrochemical measurements, an Autolab PGSTAT302N electrochemical workstation with an add-on booster was used to characterize the performance of the AEM-DAFC. Polarization curves were obtained galvanostatically, with the cell operating at each current density for one minute to reach a steady state. The cell voltage was determined by averaging the voltage over the last 10 s at each set point. Electrochemical impedance spectroscopy measurements were performed either potentiostatically or galvanostatically, with an amplitude of 15 mV and a frequency range from 1 Hz to 18 kHz at a fuel cell voltage of 0.3 V, or with an amplitude of 10 % of the operating current and a frequency range from 1 Hz to 10 kHz. The high-frequency resistance (HFR) was determined from the high-frequency intercept of the Nyquist plot with the real axis, providing the ohmic resistance. The anode potential was assessed using a CHI604E electrochemical workstation with the open-circuit potential technique. In this setup, the anode functions as the working electrode, a Hg/HgO electrode serves as the reference electrode, and the cathode acts as the counter electrode. The Hg/HgO reference electrode was placed close to the anode to ensure precise measurement of the anode potential, thereby providing a closer approximation to its true value. Consequently, the measured value effectively represents the anode potential.

2.3. Distribution of relaxation times

The DRT technique posits that the impedance spectroscopy of a random electrochemical system can be modeled as an ohmic resistance in series with an infinite number of parallel RC circuits. This approach eliminates the need for predefined electrochemical models, providing a reliable analytical capability to distinguish processes with different time constants. Under this assumption, the impedance at specific frequencies can be expressed as exponentially decayed functions [26]:

$$Z_{\mathrm{DRT}}(f) = R_0 + Z_{\mathrm{pol}}(f) = R_0 + \int_0^{\infty} \frac{g(\tau)}{1 + i2\pi f\tau} d\tau$$

Z_{DRT} represents the impedance derived from the DRT analysis; Z_{pol} stands for the polarization resistance; R_0 is the ohmic resistance; $g(\tau)$ is the time relaxation distribution function; i is the imaginary part; f is the frequency; τ represents the time constant of a single RC element.

2.4. Post-test characterization

For verification of the cell performance degradation indicated by the DRT analysis, post-test characterization was conducted to visualize the microstructure of the electrodes and variation in the composition of catalysts. The electrode after a 50-h stability test was termed as aged electrode, and a fresh electrode was made for comparison, which was termed as initial electrode. A Zeiss Sigma 300 scanning electron microscope (SEM) was used to observe the morphology of the electrode surface before and after the stability test. The elemental distributions of the electrode were observed by an Oxford Xplore 30-ray energy dispersive spectrometer (EDS).

3. Results and discussion

3.1. Identification of different polarization processes

Fig. 1 illustrates the working principle of AEM-DAFCs. At the anode, the AOR occurs, while the ORR takes place at the cathode. The movement of OH^- from the cathode to the anode forms the internal ionic current, and the movement of electrons from the anode to the cathode forms the external circuit current. In this process, the chemical energy stored in ammonia is continuously converted into electrical energy, involving various polarization processes. During cell operation, it is crucial to perform in-situ diagnostics to identify the causes of performance degradation. Combining EIS with equivalent circuit models (ECMs) offers a feasible diagnostic method. However, a single set of EIS spectra can often correspond to multiple ECMs, requiring significant expertise to select the most appropriate model, which can be confusing in practical applications. The DRT is considered a more effective technique to address these challenges. It transforms EIS spectra from the frequency domain to the time domain, providing clear characteristic peaks that represent different polarization processes. In this work, DRT analysis is applied for the first time to AEM-DAFCs, successfully converting EIS spectra into three distinct characteristic peaks. Peak 1 (P1) represents the kinetics of AOR, peak 2 (P2) stands for the kinetics of ORR, and peak 3 (P3) denotes the ionic transport. The peak areas correspond to the resistance of these processes. Peak identification was achieved by adjusting the operating conditions, as illustrated in Fig. 2. The first peak, P1, represents the kinetics of AOR and is strongly correlated with ammonia concentration, as shown in Fig. 2a. Increasing the ammonia concentration from 0.5 to 3.0 M significantly improves AOR kinetics, evidenced by the shrinking area of P1, which aligns with predictions based on the Nernst equation. The second peak, P2, corresponds to the kinetics of ORR and is sensitive to the oxygen flow rate. As depicted in Fig. 2b, increasing the oxygen flow rate from 10 SCCM to 50 SCCM decreases the P2 area, indicating enhanced ORR kinetics. However, further increasing the flow rate to 200 SCCM expands the P2 area, suggesting a deterioration in ORR kinetics. This decline is attributed to insufficient water, as the supplied oxygen is dry and the necessary water for the reaction is entirely derived from the anode. Consequently, high oxygen flow can dry out the cathode, hindering ORR kinetics. The third peak, P3, is associated with ionic transport in the catalyst layer. As shown in Fig. 2c, the P3 area significantly decreases with increased KOH concentration, as higher concentrations enhance ion transport in the anode catalyst layer, thereby reducing ionic transport resistance. Conversely, Fig. 2b shows that increasing the oxygen flow rate reduces water content in the cathode catalyst layer, which hinders transport and increases ionic transport resistance. The increased area of P3 further confirms this effect. In summary, the DRT analysis effectively distinguishes the contributions of AOR kinetics, ORR kinetics, and ionic transport to the overall performance of AEM-DAFCs, highlighting the impact of operating conditions on these processes.

3.2. Characteristics of ammonia oxidation reaction

The AOR occurs at the anode, where ammonia reacts with hydroxide ions to produce nitrogen, water and electrons. There are two proposed mechanisms for the AOR. One is the Oswin – Salomon (O – S) mechanism [33], in which ammonia (NH_3) is first adsorbed onto surface sites

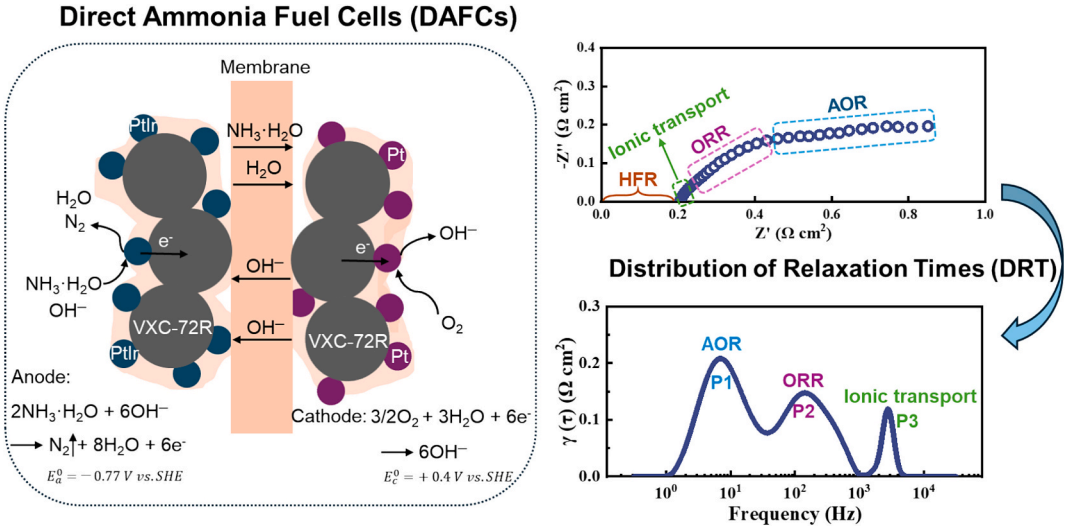

Fig. 1. Diagnosis of different polarization processes in AEM-DAFCs via DRT analysis.

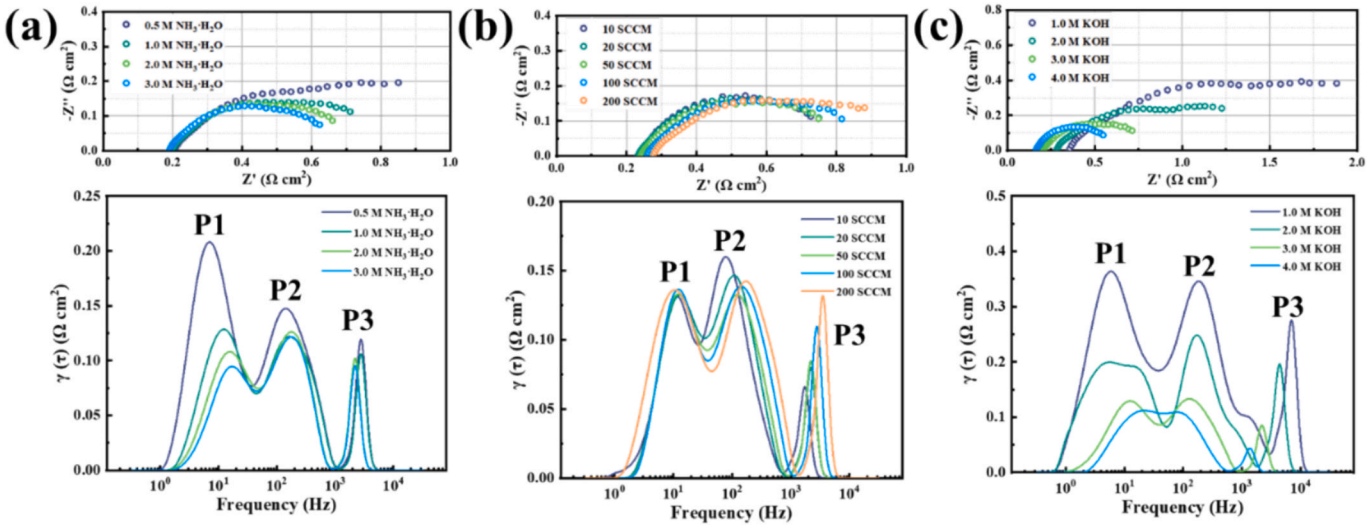

Fig. 2. DRT analysis considering the effect of (a) ammonia concentration, (b) oxygen flow rate, and (c) KOH concentration. (Anode catalyst: PtIr/C(40 %), 2.0 mg cm^{-2}. Cathode catalyst: Pt/C(60 %), 1.0 mg cm^{-2}. Membrane: PiperION A60. Fuel solution: 3.0 M (or 0.5, 1.0, 2.0 M) $NH_3{\cdot}H_2O$ in 3.0 M (or 1.0, 2.0, 4.0 M) KOH, 1.0 mL min^{-1}. Oxidant: Pure oxygen, 50 SCCM (or 10, 20, 100, 200 SCCM). Operating temperature: 80 °C.).

(*) and then undergoes sequential dehydrogenation assisted by hydroxide ions (OH^-) to form *N. Subsequently, two *N atoms dimerize on the surface to produce nitrogen. The other is the Gerischer – Mauerer (G – M) mechanism [34], which describes a different pathway. In this mechanism, ammonia (NH_3) undergoes partial dehydrogenation through its interaction with *OH, resulting in the formation of *NH_x species, where x can be 1 or 2. These *NH_x species then couple together to form *N_2H_y compounds, such as adsorbed hydrazine (*N_2H_4). Following this coupling, *N_2H_y undergoes stepwise dehydrogenation, ultimately yielding nitrogen. Platinum (Pt) is recognized as the most active single-metal catalyst for the oxidation of ammonia. Evidence suggests that the mechanism of AOR catalyzed by Pt is dependent on the applied potential [35]. At low potentials, the G – M mechanism is predominant, preventing fully dehydrogenation to *N. In contrast, at moderate to high potentials, the O – S mechanism is favored. Pt surface becomes deactivated by strongly adsorbed reaction intermediates, such as *N and *NO, when the potential exceeds 0.6 V_{RHE} [36,37]. This results in a narrow potential window where the AOR can proceed continuously, limiting the ability to increase the AOR rate by applying a higher overpotential [15]. The deactivation of the catalyst also seriously hinders the stability of AOR, especially at high potential.

Despite the AOR being extensively studied at the three-electrode level, it has rarely been examined at the device level. To explore how AOR affects the operation of AEM-DAFCs, the cell was operated at 300 mA cm^{-2} and 80 °C. The EIS with DRT analysis was used to investigate the impact of AOR kinetics degradation on cell stability. Fig. 3a shows the cell stability under these conditions. Initially, the cell voltage declines rapidly. Once it falls below 0.15 V, a sudden voltage drop occurs, accompanied by a sharp increase in anode potential, as illustrated in Fig. 3b. At cell voltages below 0.15 V (corresponding to AOR potentials exceeding 0.6 V_{RHE}, the anode catalysts experience rapid poisoning by strongly adsorbed intermediates, a phenomenon fundamentally rooted

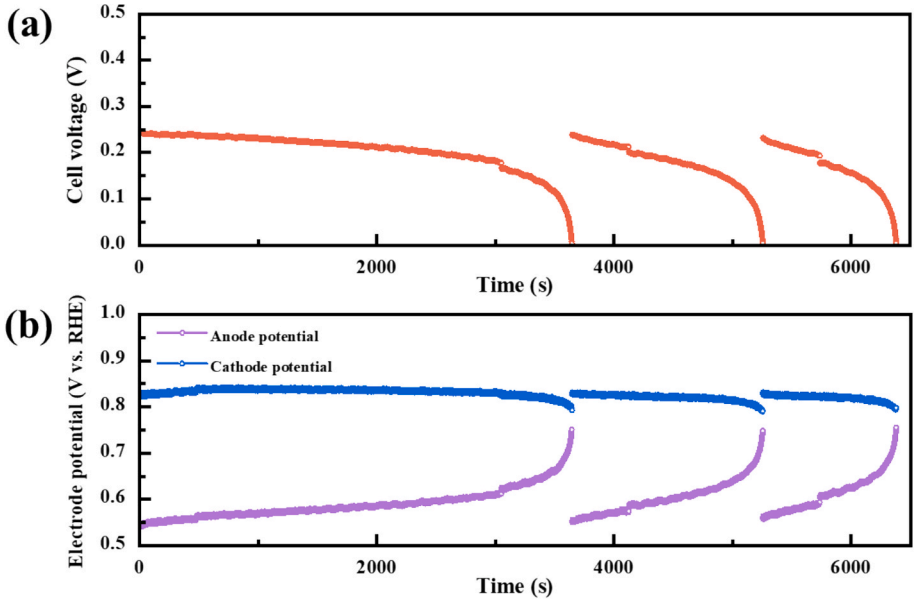

Fig. 3. Variations of (a) cell voltage and (b) anode and cathode potentials at a constant current density of 300 mA cm^{-2}. (Anode catalyst: PtIr/C(40 %), 2.0 mg cm^{-2}. Cathode catalyst: Pt/C(60 %), 2.0 mg cm^{-2}. Membrane: PiperION A60. Fuel solution: 2.0 M $NH_3{\cdot}H_2O$ in 3.0 M KOH, 2.0 mL min^{-1}. Oxidant: Pure oxygen, 50 SCCM. Operating temperature: 85 °C.).

in the O-S and G-M mechanisms. Upon restarting the cell, the initial voltage matches that of the first test, but the operation duration significantly decreases, indicating that anode poisoning comprises both reversible and irreversible mechanisms. Some intermediates induce temporary poisoning through short-term adsorption and subsequently desorb during restart, releasing active sites, while others remain permanently adsorbed, causing irreversible poisoning. Fig. 3c presents the polarization curves before and after the stability test. At a current density of 200 mA cm^{-2}, the voltage decreased by 28 mV, with more pronounced voltage decay observed at higher current densities. Analysis of the anode and cathode potential indicates that the voltage decay is primarily due to anode degradation, while cathode degradation may result from ammonia crossover, as depicted in Fig. 3d. EIS data further confirm that the performance decline is linked to a decrease in reaction kinetics, as the ohmic resistance remains nearly constant, but the semicircle associated with reaction kinetics expands significantly. DRT analysis shows that the increase in P1 is the main factor contributing to the degradation, reinforcing that the reduction in AOR kinetics caused by anode catalyst poisoning is responsible for the observed decline in cell performance, as illustrated in Fig. 4. Note that, the smaller peak on the left side of the P1 may represent the mass transfer process, as the test was conducted at a relatively high current density (300 mA cm^{-2}), where mass transfer limitations, such as the diffusion of ammonia, may become more significant.

3.3. Characteristics of oxygen reduction reaction

The ORR occurs at the cathode, where oxygen reacts with water to produce hydroxide ions. Platinum catalysts are widely used in AEM-DAFCs for ORR due to their excellent catalytic activity and stability. However, platinum also exhibits high catalytic activity for the AOR. Consequently, when ammonia cross the membrane from the anode to the cathode, AOR can occur in the cathode catalyst layer, generating parasitic currents and leading to a mixed potential. As shown in Fig. 5a, ORR half-cell tests indicate that the cathode potential, dominated by ORR, decreases from 1.08 to 0.91 V_{RHE} upon the addition of ammonia solution to the electrolyte, due to the mixed potential caused by ammonia crossover. Linear sweep voltammetry (LSV) of the cathode electrode reveals a 36 % reduction in oxygen reduction current density at 0.6 V_{RHE}, indicating a significant decrease in ORR activity, as shown in Fig. 5b. This reduction is attributed to ammonia or its oxidation intermediates blocking some of the ORR active sites. The half-cell results demonstrate that ammonia crossover severely impairs ORR.

To investigate the impact of ammonia crossover on full-cell performance, we conducted polarization curve tests, anode potential measurements (Fig. 5c and 5d), and EIS with DRT analysis (Fig. 6). Initially, at current densities exceeding 350 mA cm^{-2}, the cell voltage drops rapidly, showing significant concentration polarization. The results of anode and cathode potential measurements indicate that this polarization is due to insufficient oxygen supply. At the limiting current density, the cathode catalyst layer experiences severe oxygen deficiency, allowing ammonia from the anode to occupy the available active sites, significantly blocking ORR sites. After the first polarization curve test, a second test was conducted after the open-circuit voltage stabilized, referred to as the aged curve. The results show that ammonia crossover deteriorates cell performance, reducing peak power density by approximately 27 %. Anode and cathode potential measurements confirm that the voltage drop stems from increased cathode overpotential. EIS data reveal that performance degradation arises from impaired reaction kinetics, as the semicircle in the EIS curve of the aged fuel cell is significantly enlarged. DRT analysis further supports this, showing hindered ORR kinetics, indicated by a marked increase in the P2 peak area and a

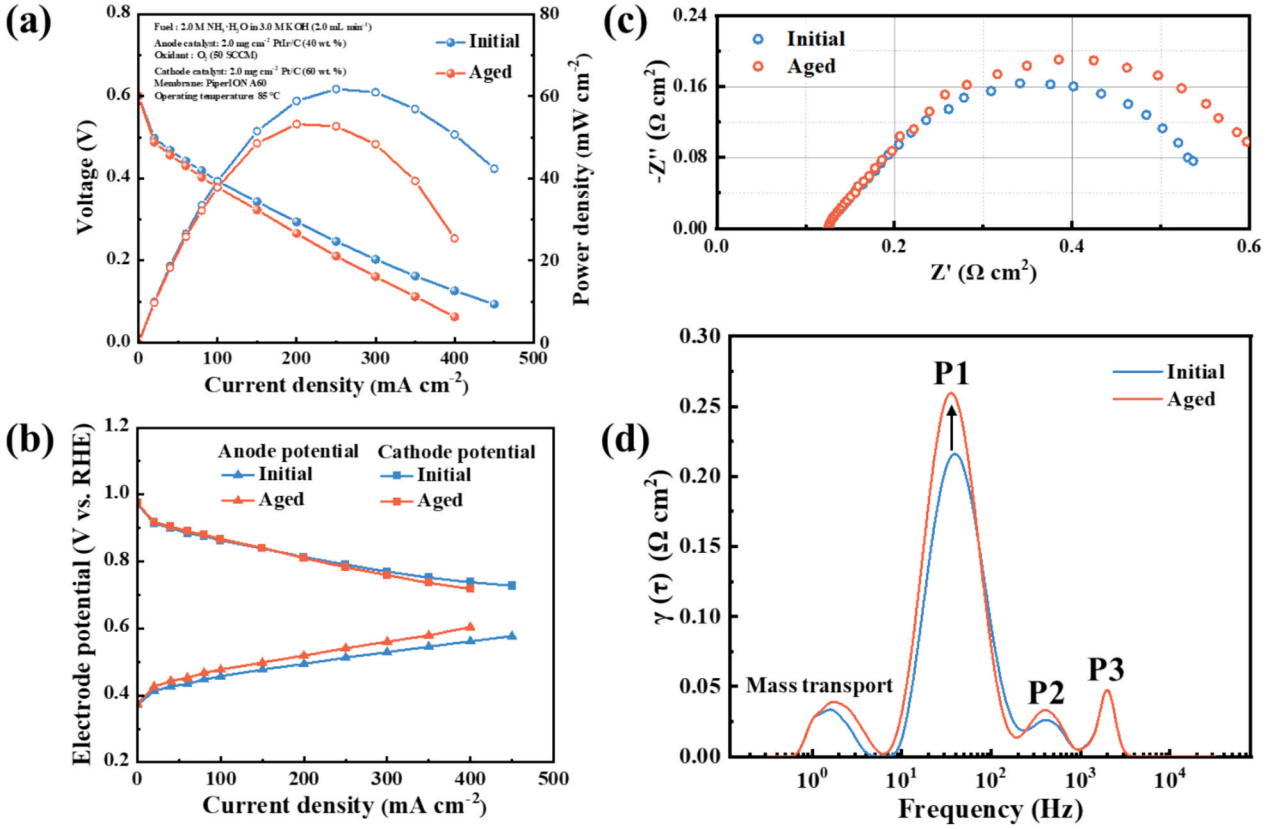

Fig. 4. (a) Polarization and power density curves. (b) Anode and cathode potential curves. (c) Nyquist plot and (d) evolution of the DRT before and after the stability test. (Anode catalyst: PtIr/C(40 %), 2.0 mg cm^{-2}. Cathode catalyst: Pt/C(60 %), 2.0 mg cm^{-2}. Membrane: PiperION A60. Fuel solution: 2.0 M $NH_3{\cdot}H_2O$ in 3.0 M KOH, 2.0 mL min^{-1}. Oxidant: Pure oxygen, 50 SCCM. Operating temperature: 85 ℃.).

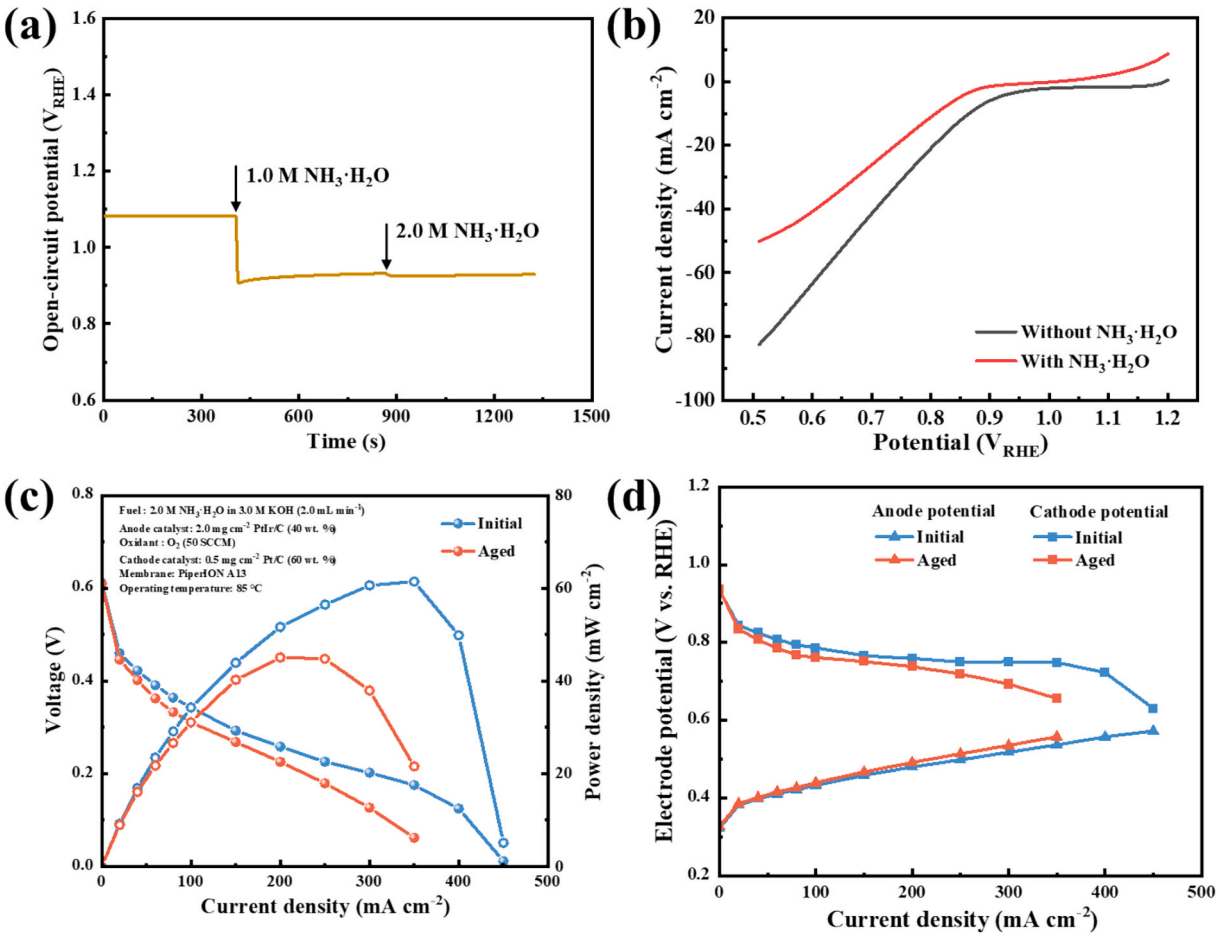

Fig. 5. Half-cell measurements of (a) the open-circuit potential and (b) linear sweep voltammetry of the cathode electrode without/with ammonia in the 1.0 M KOH anolyte solution. (c) Polarization and power density curves. (d) Anode and cathode potential curves. (Anode catalyst: PtIr/C(40 %), 2.0 mg cm^{-2}. Cathode catalyst: Pt/C(60 %), 0.5 mg cm^{-2}. Membrane: PiperION A13. Fuel solution: 2.0 M $NH_3·H_2O$ in 3.0 M KOH, 2.0 mL min^{-1}. Oxidant: Pure oxygen, 50 SCCM. Operating temperature: 85 ℃.).

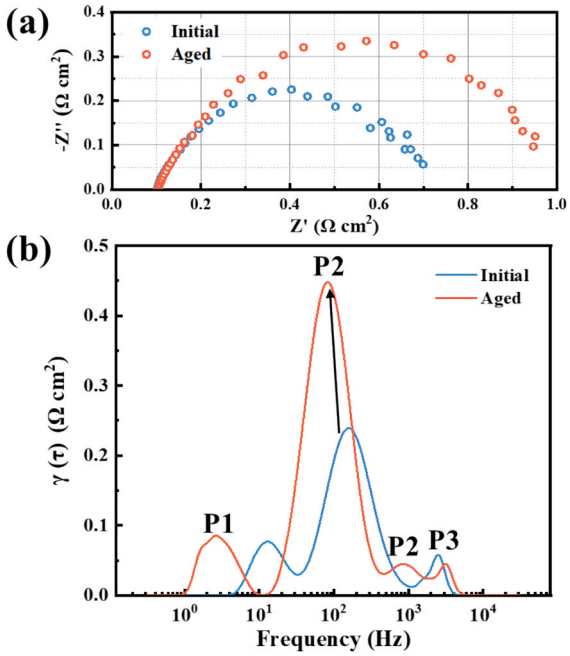

Fig. 6. (a) Nyquist plot and (b) evolution of the DRT before and after the stability test.

shift of its characteristic frequency toward lower frequencies. The increase in P2 peak area results from severe ammonia crossover, which causes the cathode catalyst to be occupied by ammonia or intermediates from ammonia oxidation, reducing the active sites available for ORR. This worsens ORR kinetics, slowing the reaction rate at the electrode surface and lengthening relaxation time, thus shifting the P2 characteristic frequency to lower values. This section is the first to demonstrate at the device scale that ammonia crossover obstructs cathode ORR in AEM-DAFCs, highlighting the importance of developing ammonia-tolerant ORR catalysts.

3.4. Long-term stability test

A 50-hour stability test was conducted to investigate the degradation mechanism of the AEM-DAFC. Fig. 7a shows that the cell voltage decreased from 0.445 V to 0.371 V, with a decay rate of 1.48 mV h^{-1}. Fig. 7b indicates that the anode potential increased by nearly 62 mV (accounting for 85 % of the total change), while the cathode potential decreased by only 9 mV (accounting for 12 %). This clearly demonstrates that the increase in anode potential is the primary factor contributing to the cell voltage degradation. Additionally, Fig. 7b shows that the ohmic overpotential is negligible, indicating that the performance of the AEM-DAFCs is mainly determined by the combined effects of anode and cathode overpotentials.

Polarization curves and anode potential measurements were conducted before and after the 50-hour stability test, as shown in Fig. 7c. The peak power density of the cell declined by 51 %, which can be

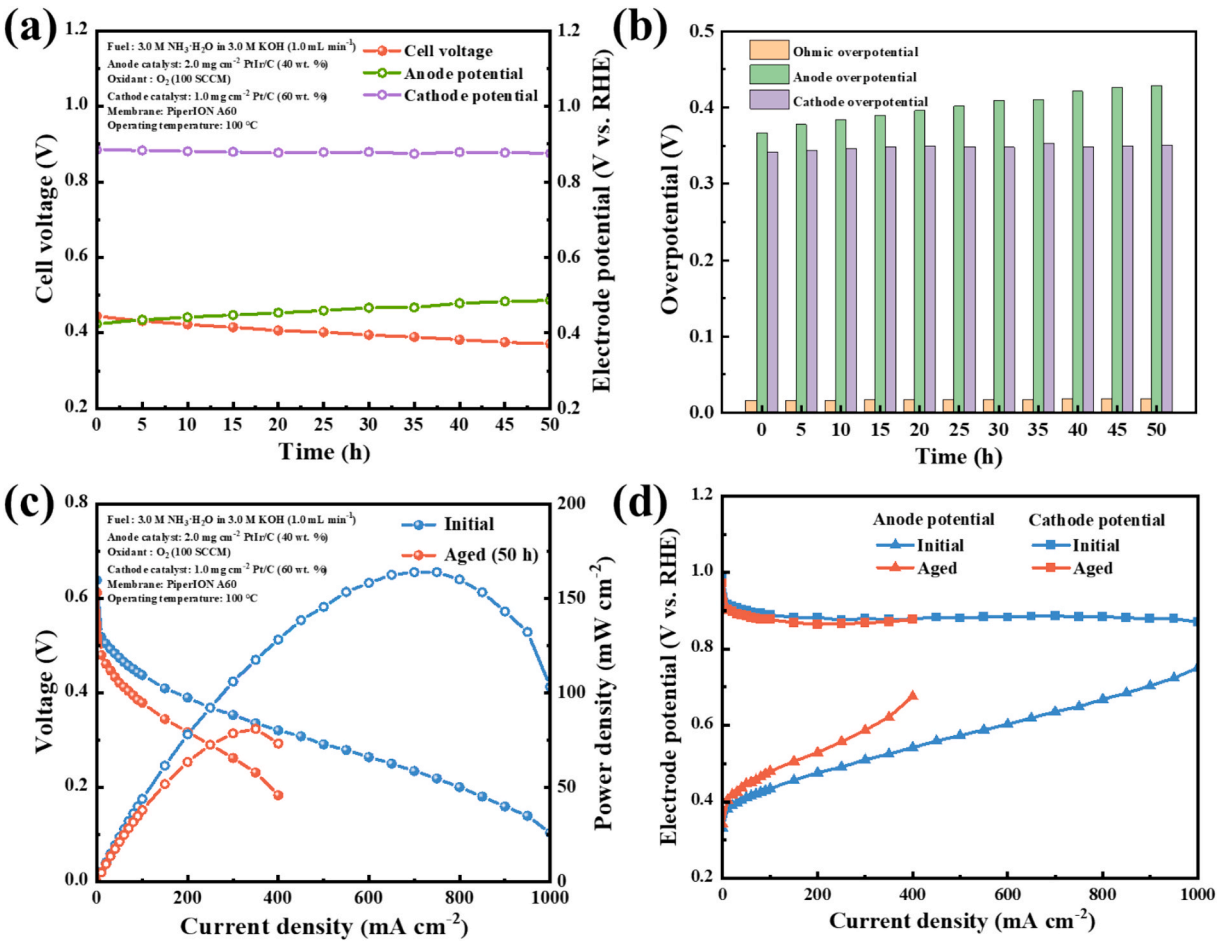

Fig. 7. Variations of (a) cell voltage, anode and cathode potentials at a constant current density of 100 mA cm^{-2}. (b) Breakdown of overpotentials. (c) Polarization and power density curves. (d) Anode and cathode potential curves. (Anode catalyst: PtIr/C(40 %), 2.0 mg cm^{-2}. Cathode catalyst: Pt/C(60 %), 1.0 mg cm^{-2}. Membrane: PiperION A60. Fuel solution: 3.0 M $NH_3 \cdot H_2O$ in 3.0 M KOH, 1.0 mL min^{-1}. Oxidant: Pure oxygen, 100 SCCM. Operating temperature: 100 °C.).

attributed to the degradation of the anode electrode. Electrode potential data indicated that the cathode potential remained almost unchanged, whereas the anode potential increased significantly, leading to a rise in anode overpotential (Fig. 7d). This is further confirmed by the EIS data with DRT analysis presented in Fig. 8, where the area of peak P1 increased significantly while other characteristic peaks remained nearly the same. This implies that the degradation in cell performance is due to a reduction in the AOR kinetics.

3.5. Post-test characterization

As discussed in previous sections, the degradation of the anode electrode is a primary factor affecting cell stability. In this section, post-test characterization tests are conducted to investigate the causes of anode electrode degradation. The SEM results in Fig. 9a and 9b show significant agglomeration of catalyst particles after stability testing, leading to a reduction in active sites and subsequent anode electrode degradation. Fig. 10 indicates that the electrochemical surface area (ECSA) decreased by nearly 46 %. EDS analysis in Fig. 9c and 9d further reveals that catalyst dissolution occurred during stability testing, with the atomic ratio of Pt to Ir changing from 54.63:45.37 to 69.23:30.77, indicating more severe dissolution of Ir. The reduction in ECSA is attributed not only to catalyst dissolution and migration but also to the occupation of active sites by AOR intermediates. A cleaning procedure (Cyclic Voltammetry measurements in Ar-saturated 1.0 M KOH solution at a scan rate of 100 mV s^{-1} for 100 cycles) was applied to the anode electrode, and Fig. 10 shows that after cleaning, the ECSA increased, suggesting that some AOR intermediates adsorbed on active sites were removed, partially restoring the active sites. However, according to the literatures [14,15], not all adsorbed poisoning species can be removed by this cleaning procedure. In summary, the degradation of the anode electrode is caused by catalyst particle dissolution, migration, agglomeration, and poisoning by AOR intermediates such as *N and *NO_x.

4. Conclusions

This study investigates the degradation mechanisms of AEM-DAFCs using in-situ EIS and reference electrode measurements to decouple overpotential losses. Moreover, DRT analysis is applied to separate overlapping polarization processes in EIS spectra. Additionally, a 50-hour stability test assesses the long-term viability of AEM-DAFCs, while pre- and post-test characterization reveals microstructural and compositional changes in the electrodes. These combined analyses yield the following key conclusions:

1. The DRT analysis reveals three distinct polarization losses: AOR kinetics, ORR kinetics and ionic transport.
2. The poisoning effect of AOR under high electrode potential constrains the operating window of AEM-DAFCs, and when the anode potential exceeds 0.6 V (vs. RHE), the cell voltage may undergo a sharp deterioration.
3. During 50-h stability testing at 100 mA cm^{-2}, the cell voltage declined from 0.445 to 0.371 V with a decay rate of 1.48 mV h^{-1}. The deterioration of AOR kinetics is the main factor responsible for cell

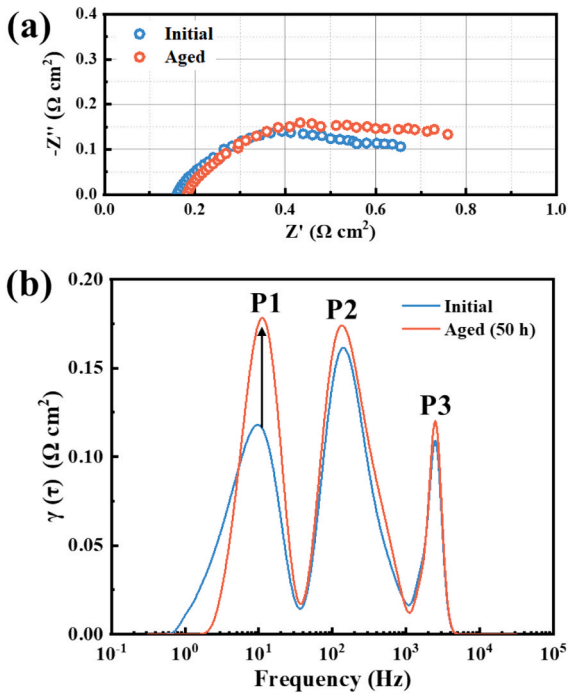

Fig. 8. (a) Nyquist plot and (b) evolution of the DRT before and after the stability test.

performance deterioration, as anode overpotential increased by 62 mV (accounting for 85 % of the cell voltage decay).

4. The degradation of anode electrode was demonstrated by a reduction (46 %) in ECSA. SEM images clearly shown severe catalyst loss and agglomeration. EDS revealed a Pt/Ir ratio shift from 55:45 to 69:31, confirming preferential Ir dissolution. The 17 % ECSA recovery after electrode cleaning verified catalyst poisoning by adsorbed species (*N/*NO_x), collectively causing electrode deterioration.

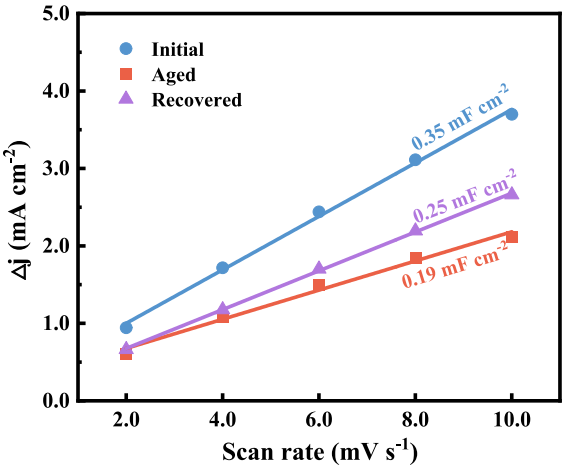

Fig. 10. Half of the difference in current density at −0.43 V (vs. Hg/HgO) versus scan rate for the anode electrode.

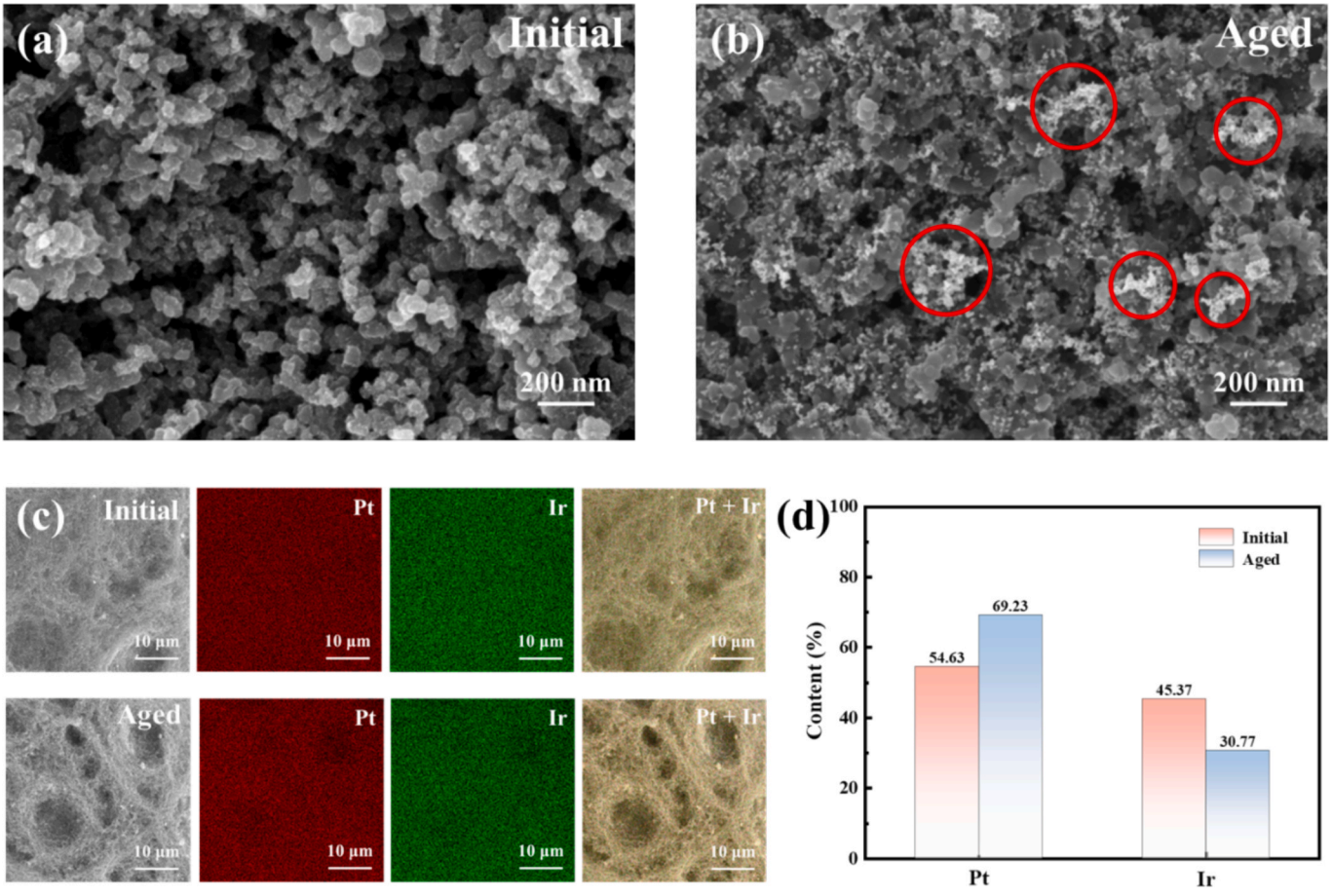

Fig. 9. SEM characterization of the anode electrode (a) before and (b) after the 50-h stability test. (c) EDX elemental mappings. (d) Variations of Pt and Ir contents.

Further research is necessary to develop highly efficient and stable catalysts for the ammonia oxidation reaction. Such advancements would alleviate the poisoning caused by reaction intermediates and inhibit the dissolution and loss of catalyst metals. Consequently, these improvements will significantly contribute to enhancing the stability of AEM-DAFCs.

CRediT authorship contribution statement

Wenzhi Li: Writing – original draft, Methodology, Investigation. **Qing Wang:** Software, Methodology. **Yun Liu:** Writing – review & editing, Methodology. **Lizhen Wu:** Software, Methodology. **Zhefei Pan:** Writing – review & editing, Investigation. **Rong Chen:** Writing – review & editing. **Liang An:** Writing – review & editing, Supervision, Project administration, Funding acquisition.

Declaration of competing interest

The authors declare that they have no known competing financial interests or personal relationships that could have appeared to influence the work reported in this paper.

Acknowledgement

The work described in this paper was supported by a grant from the Research Grants Council of the Hong Kong Special Administrative Region, China (N_PolyU559/21), a grant from the National Natural Science Foundation of China (52161160333), and a grant from the Research Institute for Smart Energy (CDB2) at The Hong Kong Polytechnic University.

Appendix A. Supplementary data

Supplementary data to this article can be found online at https://doi.org/10.1016/j.cej.2025.162204.

Data availability

Data will be made available on request.

References

[1] G. Jeerh, M. Zhang, S. Tao, Recent progress in ammonia fuel cells and their potential applications, J. Mater. Chem. A 9 (2021) 727–752, https://doi.org/10.1039/D0TA08810B.
[2] B. Wang, T. Li, F. Gong, M.H.D. Othman, R. Xiao, Ammonia as a green energy carrier: Electrochemical synthesis and direct ammonia fuel cell - a comprehensive review, Fuel Process. Technol. 235 (2022) 107380, https://doi.org/10.1016/j.fuproc.2022.107380.
[3] W. Li, Y. Liu, Z. Zhang, Z. Pan, R. Chen, L. An, Performance of a hybrid direct ammonia fuel cell with hydrogen peroxide reduction, J. Power Sources 593 (2024) 233985, https://doi.org/10.1016/j.jpowsour.2023.233985.
[4] H. Zhang, K. Xu, F. He, F. Zhu, Y. Zhou, W. Yuan, Y. Liu, M. Liu, Y. Choi, Y. Chen, Challenges and Advancements in the Electrochemical Utilization of Ammonia Using Solid Oxide Fuel Cells, Adv. Mater. 36 (2024) 2313966, https://doi.org/10.1002/adma.202313966.
[5] Y. Zhao, B.P. Setzler, J. Wang, J. Nash, T. Wang, B. Xu, Y. Yan, An Efficient Direct Ammonia Fuel Cell for Affordable Carbon-Neutral Transportation, Joule 3 (2019) 2472–2484, https://doi.org/10.1016/j.joule.2019.07.005.
[6] R. Lan, S. Tao, Direct Ammonia Alkaline Anion-Exchange Membrane Fuel Cells, Electrochem. Solid-State Lett. 13 (2010) B83, https://doi.org/10.1149/1.3428469.
[7] Y. Guo, Z. Pan, L. An, Carbon-free sustainable energy technology: Direct ammonia fuel cells, J. Power Sources 476 (2020) 228454, https://doi.org/10.1016/j.jpowsour.2020.228454.
[8] J. Wang, Y. Zhao, B.P. Setzler, S. Rojas-Carbonell, C. Ben Yehuda, A. Amel, M. Page, L. Wang, K. Hu, L. Shi, S. Gottesfeld, B. Xu, Y. Yan, Poly(aryl piperidinium) membranes and ionomers for hydroxide exchange membrane fuel cells, Nat Energy 4 (2019) 392–398, https://doi.org/10.1038/s41560-019-0372-8.
[9] T. Wang, Y. Zhao, B.P. Setzler, R. Abbasi, S. Gottesfeld, Y. Yan, A high-performance 75 W direct ammonia fuel cell stack, Cell Rep. Phys. Sci. 3 (2022) 100829, https://doi.org/10.1016/j.xcrp.2022.100829.
[10] Y. Liu, Z. Pan, O.C. Esan, X. Xu, L. An, Performance Characteristics of a Direct Ammonia Fuel Cell with an Anion Exchange Membrane, Energy Fuels 36 (2022) 13203–13211, https://doi.org/10.1021/acs.energyfuels.2c02951.
[11] T. Wang, Y. Zhao, B.P. Setzler, Y. Yan, Improving Performance and Durability of Low Temperature Direct Ammonia Fuel Cells: Effect of Backpressure and Oxygen Reduction Catalysts, J. Electrochem. Soc. 168 (2021) 014507, https://doi.org/10.1149/1945-7111/abdcca.
[12] X. Du, A. Du, D. Wang, Y. Mao, Z. Zhang, W., Xie, Surface-Enhanced Raman Spectroscopic Study of Key Intermediates in Electrochemical Ammonia Decomposition, J. Am. Chem. Soc. (2024) jacs.4c15489, https://doi.org/10.1021/jacs.4c15489.
[13] H. Wang, D.R. Dekel, H.D. Abruña, Unraveling the Mechanism of Ammonia Electrooxidation by Coupled Differential Electrochemical Mass Spectrometry and Surface-Enhanced Infrared Absorption Spectroscopic Studies, J. Am. Chem. Soc. (2024), https://doi.org/10.1021/jacs.4c02621.
[14] Z.-F. Li, Y. Wang, G.G. Botte, Revisiting the electrochemical oxidation of ammonia on carbon-supported metal nanoparticle catalysts, Electrochim. Acta 228 (2017) 351–360, https://doi.org/10.1016/j.electacta.2017.01.020.
[15] H. Kim, W. Yang, W.H. Lee, M.H. Han, J. Moon, C. Jeon, D. Kim, S.G. Ji, K.H. Chae, K.-S. Lee, J. Seo, H.-S. Oh, H. Kim, C.H. Choi, Operando Stability of Platinum Electrocatalysts in Ammonia Oxidation Reactions, ACS Catal. 10 (2020) 11674–11684, https://doi.org/10.1021/acscatal.0c02413.
[16] K. Zhang, Y. Han, Y. Zhao, T. Wei, J. Fu, Z. Ren, X. Xu, L. Zhou, Z. Shao, Energy-efficient and cost-effective ammonia electrolysis for converting ammonia to green hydrogen, CR-PHYS-SC 5 (2024), https://doi.org/10.1016/j.xcrp.2024.102171.
[17] W. Li, Y. Liu, M. Luo, X. Shi, Z. Pan, R. Chen, L. An, Monitoring ammonia and water transport through anion exchange membranes in direct ammonia fuel cells, J. Power Sources 628 (2025) 235900, https://doi.org/10.1016/j.jpowsour.2024.235900.
[18] Z. Jiao, Y. Zhao, Y. Han, Z. Ren, J. Yang, Z. Shao, Macromolecule crosslinked hydroxide exchange membranes with low ammonia crossover for direct ammonia fuel cells, J. Membr. Sci. 722 (2025) 123862, https://doi.org/10.1016/j.memsci.2025.123862.
[19] Y. Han, Y. Zhao, Z. Ren, T. Wei, H. Zhang, S. Sun, H. Yu, Z. Shao, Studies on ammonia crossover behavior of hydroxide exchange membranes for direct ammonia fuel cells, J. Membr. Sci. 717 (2025) 123638, https://doi.org/10.1016/j.memsci.2024.123638.
[20] S. Wang, J. Zhang, O. Gharbi, V. Vivier, M. Gao, M.E. Orazem, Electrochemical impedance spectroscopy, Nat Rev Methods Primers 1 (2021) 1–21, https://doi.org/10.1038/s43586-021-00039-w.
[21] D.D. Macdonald, Reflections on the history of electrochemical impedance spectroscopy, Electrochim. Acta 51 (2006) 1376–1388, https://doi.org/10.1016/j.electacta.2005.02.107.
[22] F. Santoni, A. De Angelis, A. Moschitta, P. Carbone, M. Galeotti, L. Cinà, C. Giammanco, A. Di Carlo, A guide to equivalent circuit fitting for impedance analysis and battery state estimation, J. Storage Mater. 82 (2024) 110389, https://doi.org/10.1016/j.est.2023.110389.
[23] X. Lai, Y. Zheng, T. Sun, A comparative study of different equivalent circuit models for estimating state-of-charge of lithium-ion batteries, Electrochim. Acta 259 (2018) 566–577, https://doi.org/10.1016/j.electacta.2017.10.153.
[24] V. Vivier, M.E. Orazem, Impedance Analysis of Electrochemical Systems, Chem. Rev. 122 (2022) 11131–11168, https://doi.org/10.1021/acs.chemrev.1c00876.
[25] S. Dierickx, A. Weber, E. Ivers-Tiffée, How the distribution of relaxation times enhances complex equivalent circuit models for fuel cells, Electrochim. Acta 355 (2020) 136764, https://doi.org/10.1016/j.electacta.2020.136764.
[26] Q. Wang, Z. Hu, L. Xu, J. Li, Q. Gan, X. Du, M. Ouyang, A comparative study of equivalent circuit model and distribution of relaxation times for fuel cell impedance diagnosis, Int. J. Energy Res. 45 (2021) 15948–15961, https://doi.org/10.1002/er.6825.
[27] X. Zhang, L. Huang, Y. Jiang, L. Lin, H. Liao, W. Liu, Investigation of nonlinear accelerated degradation mechanism in fuel cell stack under dynamic driving cycles from polarization processes, Appl. Energy 355 (2024) 122286, https://doi.org/10.1016/j.apenergy.2023.122286.
[28] P. Ren, P. Pei, Y. Li, Z. Wu, D. Chen, S. Huang, Degradation mechanisms of proton exchange membrane fuel cell under typical automotive operating conditions, Prog. Energy Combust. Sci. 80 (2020) 100859, https://doi.org/10.1016/j.pecs.2020.100859.
[29] X. Chen, L. Li, M. Liu, T. Huang, A. Yu, Detection of lithium plating in lithium-ion batteries by distribution of relaxation times, J. Power Sources 496 (2021) 229867, https://doi.org/10.1016/j.jpowsour.2021.229867.
[30] Y. Zhao, S. Kücher, A. Jossen, Investigation of the diffusion phenomena in lithium-ion batteries with distribution of relaxation times, Electrochim. Acta 432 (2022) 141174, https://doi.org/10.1016/j.electacta.2022.141174.
[31] Y. Li, Y. Jiang, J. Dang, X. Deng, B. Liu, J. Ma, F. Yang, M. Ouyang, X. Shen, Application of distribution of relaxation times method in polymer electrolyte membrane water electrolyzer, Chem. Eng. J. 451 (2023) 138327, https://doi.org/10.1016/j.cej.2022.138327.
[32] M. Ranz, B. Grabner, B. Schweighofer, H. Wegleiter, A. Trattner, Dynamics of anion exchange membrane electrolysis: Unravelling loss mechanisms with electrochemical impedance spectroscopy, reference electrodes and distribution of relaxation times, J. Power Sources 605 (2024) 234455, https://doi.org/10.1016/j.jpowsour.2024.234455.
[33] H.G. Oswin, M. Salomon, The anodic oxidation of ammonia at platinum black electrodes in aqueous koh electrolyte, Can. J. Chem. 41 (1963) 1686–1694, https://doi.org/10.1139/v63-243.

[34] H. Gerischer, A. Mauerer, Untersuchungen Zur anodischen Oxidation von Ammoniak an Platin-Elektroden, J. Electroanal. Chem. Interfacial Electrochem. 25 (1970) 421–433, https://doi.org/10.1016/S0022-0728(70)80103-6.
[35] H.S. Pillai, H. Xin, New Insights into Electrochemical Ammonia Oxidation on Pt (100) from First Principles, Ind. Eng. Chem. Res. 58 (2019) 10819–10828, https://doi.org/10.1021/acs.iecr.9b01471.
[36] F. Du, W. Sun, H. Luo, C.M. Li, Recent progress in electrochemical synthesis of carbon-free hydrogen carrier ammonia and ammonia fuel cells: A review, Mater. Rep.: Energy 2 (2022) 100163, https://doi.org/10.1016/j.matre.2022.100163.
[37] S.I. Venturini, D.R. Martins de Godoi, J. Perez, Challenges in Electrocatalysis of Ammonia Oxidation on Platinum Surfaces: Discovering Reaction Pathways, ACS Catal. 13 (2023) 10835–10845, https://doi.org/10.1021/acscatal.3c00677.